

Shape-based coordination in locomotion control

The International Journal of
Robotics Research
1–16

© The Author(s) 2018

Reprints and permissions:

sagepub.co.uk/journalsPermissions.nav

DOI: 10.1177/0278364918761569

journals.sagepub.com/home/ijr



Matthew Travers, Julian Whitman and Howie Choset

Abstract

Highly articulated systems are capable of executing a variety of behaviors by coordinating their many internal degrees of freedom to help them move more effectively in complex terrains. However, this inherent variety poses significant challenges that have been the subject of a great deal of previous work: What are the most effective or most efficient methods for achieving the intrinsic coordination necessary to produce desired global objectives? This work takes these questions one step further, asking how different levels of coordination, which we quantify in terms of kinematic coupling, affect articulated locomotion in environments with different degrees of underlying structure. We introduce shape functions as the analytical basis for specifying kinematic coupling relationships that constrain the relative motion among the internal degrees of freedom for a given system during its nominal locomotion. Furthermore, we show how shape functions are used to derive shape-based controllers (SBCs) that manage the compliant interaction between articulated bodies and the environment while explicitly preserving the inter-joint coupling defined by shape functions. Initial experimental evidence provides a comparison of the benefits of different levels of coordination for two separate platforms in environments with different degrees of inherent structure. The experimental results show that decentralized implementations, where there is relatively little inter-joint coupling, perform well across a spectrum of different terrains but that there are potential benefits to higher degrees of coupling in structured terrains. We discuss how this observation has implications related to future planning and control approaches that actively “tune” their underlying structure by dynamically varying the assumed level of coupling as a function of task specification and local environmental conditions.

Keywords

Articulated locomotion, compliant control, shape function, kinematic synergies, snake robot, hexapod robot, central pattern generator (CPG), dynamic movement primitive (DMP), admittance control

1. Introduction

Whether biological or man made, highly articulated systems are capable of leveraging fixed motion patterns that coordinate their many internal degrees of freedom to help them move more effectively in non-trivial tasks and environments. In particular, prior work shows that the expressive global behaviors of articulated systems can in many cases be represented using low-dimensional parameterized expressions that capture the coordination among their internal degrees of freedom; this has been shown in data collected from biological systems (Gong et al., 2014; Santello et al., 1998; Alexandrov et al., 1998; Freitas et al., 2006; Tricon et al., 2007) and has been demonstrated on different robotic platforms (Hauser et al., 2007, 2011; Ajoudani et al., 2013; Gabbicini et al., 20011; Catalano et al., 2012; Ciocarlie et al., 2007). However, relatively little attention has been paid to evaluating how *varying the level of coordination*, i.e. changing the total number and distribution of coordinated degrees of freedom, affects a given system’s

performance in different tasks, environments, or as the structure of the system itself changes over time. This work, thus, specifically focuses on the benefits and drawbacks that different levels of coordination have on the locomotion control of articulated robots moving through different terrains.

We introduce *shape functions* as the analytical basis for varying coordination in this work. Shape functions are parameterized expressions that define the joint-level kinematic trajectories that, under nominal conditions, produce desired locomotive modes. More specifically, shape functions are specified in terms of a set of *shape bases* and an associated set of scalar *shape parameters*. The shape

The Robotics Institute, Carnegie Mellon University, Pittsburgh, PA, USA

Corresponding author:

Matthew Travers, The Robotics Institute, Carnegie Mellon University, Pittsburgh, PA 15232, USA.

Email: mtravers@andrew.cmu.edu

bases define constraints that fix the relationship between, or rather couple, the relative motion of different combinations of a given system’s joints. Depending on the level of assumed coupling, shape functions therefore make it possible to reduce the effective size of the internal configuration space necessary to coordinate a given system’s intrinsic motions. In other words, shape functions provide the means to perform dimensionality reduction in a way that is related to pre-existing approaches (Hauser et al., 2007; Ajoudani et al., 2013; Gabbicini et al., 20011; Catalano et al., 2012; Gelfand et al., 1996; Ciocarlie et al., 2007; Hauser et al., 2011). However, we show that by identifying families of related shape functions, that *incrementally* vary their respective levels of coupling, we are able to directly and coherently evaluate how different degrees of dimensionality reduction affect the locomotion of specific platforms in different terrains.

When deployed in uncertain, complex, or possibly dynamic environments, articulated platforms seldom ever operate under nominal conditions. Therefore, instead of searching for entirely new motions that satisfy sets of perceived environmental constraints, this work develops an admittance-inspired control framework that continuously *adapts* a given system’s nominal locomotion, specified in terms of its shape function, based on proprioceptively sensed feedback. Specifically, we derive compliant control laws on the space of shape parameters; what we refer to as shape-based controllers (SBCs). The benefit of SBCs is that they assure the intrinsic joint-to-joint coordination defined by a given shape function is explicitly “built in” to the forceful adaptation of a given system’s motion to unexpected external perturbations. We show how shape functions are used to analytically map measured joint torques into equivalent *shape forces*, thus defining “force feedback” in the space of shape parameters. Furthermore, we discuss how the admittance-inspired SBCs are interpreted as *shape-based dynamic movement primitives* (DMPs) (Schaal et al., 2000, 2007; Ijspeert et al., 2002, 2013; Hogan and Sternad, 2013). Finally, we provide several examples that discuss the relationship between shape functions, SBCs, and central pattern generators (CPGs) (Ijspeert et al., 2013; Ijspeert, 2008; Ijspeert and Kodjabachian, 1999; Ijspeert and Crespi, 2007; Zhang et al., 2014; Campos et al., 2010; Pinto, 2012).

The main contribution of this work shows that by defining shape functions with different levels of coupling for the same platform, that vary from the fully coupled (where each joint in the system is kinematically linked through a single shape basis) to fully decoupled (where each joint is independent), makes it possible to derive a family of SBCs that vary in their extent of control decentralization (Siciliano et al., 2009). We present initial experimental results for the two platforms shown in Figure 1 that compare the benefits of SBCs with different levels of decentralization in both a regularized environment, such as a staircase with uniform step width, and in an environment with random features, such as a pile of rocks. We find that centralized controllers



Fig. 1. Modular snake-like and hexapod robots used in the examples and experiments presented in this work.

(with a high level of coupling) perform well in structured terrains, whereas highly decentralized controllers (with a high level of decoupling) perform well across different environmental conditions and offer significant advantages in unstructured terrains. This work supports the belief that our experimental results show there are potential benefits to “tunable dimensionality” in the SBC framework. We discuss the future implications we believe these benefits will have on balancing functionality and computational complexity in the control of and motion planning for articulated systems.

To better support our experimental results, and to provide a more general context for the “shape-based” approach presented in this work, we introduce in Section 2 prior work on modal shape functions, kinematic synergies, admittance control, DMPs, and CPGs. We use the presentation of this prior work to help motivate the introduction of shape functions and SBCs in Section 3. We then provide several examples that highlight the implementation details of SBCs in Section 4. These examples show how shape functions with different levels of kinematic coupling affect the performance of their resulting SBCs. The main experimental results of this work and a discussion of our findings are presented in Section 5. Finally, a summary of shape functions, SBCs, our examples, and experimental results, as well as the future direction of this work are presented in Section 6.

2. Related work

Shape functions and SBCs are inspired by previous work on *modal* shape functions, kinematic synergies, admittance

control, and DMPs/CPGs. Each of these topics is briefly introduced.

2.1. Modal shape functions

In Section 4, we present several examples of shape functions for the snake-like robot shown in Figure 1. Each of the snake-like robot shape functions are closely related to the *modal shape functions* originally introduced by Chirikjian and Burdick (1991, 1994). This previous work originally focused on fixed-base continuum manipulators modeled using three-dimensional backbone curves. A backbone curve reference set shape function was defined by Chirikjian and Burdick (1994) in terms of four geometric parameters (that represent a Frenet–Serret frame, for example (Do Carmo, 1976; Yamada and Hirose, 2006)), $S_i(s, t) \in \mathbb{R}$, where $i = \{1, 2, 3, 4\}$, and s is a continuous arc length. Furthermore, each $S_i(s, t)$ was defined such that

$$S_i(s, t) = \sum_{j=1}^N a_{ij}(t) \phi_{ij}(s) \quad (1)$$

where $\phi_{ij}(s)$ represent modal functions, $a_{ij}(t)$ are the “modal participation factors,” and N is the total number of modes. The modal representations in (1) were used by Chirikjian and Burdick (1991, 1994) to help simplify inverse kinematics problems for continuum manipulators, effectively reducing the problem from an infinite-dimensional optimization to an optimization over the finite set of modal participation factors. A similar approach was applied to derive the kinematics of a sidewinding snake model by Burdick et al. (1993).

2.2. Kinematic synergies

Similar to previous approaches (Hauser et al., 2007, 2011; Ajoudani et al., 2013; Gabbicini et al., 20011; Catalano et al., 2012; Ciocarlie et al., 2007; Prattichizzo et al., 2006), this work defines kinematics synergies in terms of functions f that map scalar parameters $\sigma(t) \in \mathbb{R}$ into N -dimensional joint spaces, i.e. $f : \mathbb{R} \rightarrow \mathbb{R}^N$, where we assume the joint angles $\theta \in \mathbb{R}^N$.¹ Furthermore, we assume each mapping f is defined by a static basis vector $\beta \in \mathbb{R}^N$ such that $f(\sigma(t)) = \sigma(t) \beta$. Note that, depending on the definition of β , changes in the synergy parameters $\sigma(t)$ can coordinate the motion across potentially large collections of a system’s joints. Thus, as previous work shows (Ciocarlie et al., 2007; Ficuciello et al., 2011), low-dimensional collections of synergies, e.g. $(f_1(\sigma_1(t)), f_2(\sigma_2(t)), \dots, f_M(\sigma_M(t)))$, where $M < N$, can be used to coordinate relatively articulate motions for high-degree-of-freedom systems; in this sense, kinematic synergies make it possible to perform dimensionality reduction. Note that the concept of muscle synergies, which are related to kinematic synergies in the sense that they provide evidence that low-dimensional activation signals are used to coordinate complex, multi-degree-of-freedom motions, have been studied quite extensively by the

neuroscience community; see Ting and Macpherson (2004) and d’Avella et al. (2006) as well as the references therein.

Kinematic synergies are thus closely related to the modal shape functions in (1), where the “motion” of the infinite-dimensional backbone curves are coordinated using finite collections of the modal participation factors $a_{ij}(t)$. The main differences between the two are that synergies are directly defined for discrete joint spaces and easily extend to general topologies, whereas previous work on modal approaches focused on continuum systems with serial topologies.

In addition, previous work by Prattichizzo et al. (2006), Gabbicini et al. (20011), Wimboeck et al. (2011), and Catalano et al. (2012) developed different aspects of force control methods defined directly in terms of *postural synergies*. These previous works are related to the SBCs that are introduced in Section 3.2. However, Prattichizzo et al. (2006), Gabbicini et al. (20011), Wimboeck et al. (2011), and Catalano et al. (2012) focused primarily on manipulation and the explicit control of the extrinsic forces applied by a manipulator on different objects. We show in the remainder of this work that SBCs provide a fundamentally intrinsic force-control approach that relies on very little information about the environment and is designed specifically for locomotion control in complex terrains.

Lastly, we note that an important topic in previous work on both modal shape functions as well as synergies, that is not directly addressed for shape functions in this work, is how they are derived. For example, Gong et al. (2014) extracted low-dimensional expressions from biological snake data using multi-dimensional singular-value decomposition (SVD) to derive modal-shape bases for different locomotive behaviors. Godage et al. (2015) used a Taylor expansion to analytically derive modal shape functions for highly articulated manipulators. Santello et al. (1998) also used SVD, but applied it to human grasping data to numerically derive bases for a space of postural synergies. Hauser et al. (2007, 2011) used offline optimization to derive whole-body synergies for a humanoid balancing model. We make the claim that these previous works provide a roadmap of different methods that can be applied to derive shape functions similar to those presented in this work. A further discussion related to future methods for automating the derivation of shape functions is presented in Section 6.

2.3. Admittance control

The SBC framework presented in Section 3.2 is inspired by, and in special cases directly related to, conventional admittance control (Hogan, 1985; Lawrence, 1988). In the broader context of force control methods, admittance control is an indirect approach that takes in a force (or torque) measurement and returns a desired position command. This desired command is then tracked by a low-level position-based controller.

For example, consider a fixed-base manipulator with N internal degrees of freedom, $\theta \in \mathbb{R}^N$. The closed-loop dynamics for the manipulator and its associated admittance controller are, respectively,

$$\ddot{\theta} + k_d \dot{\theta} + k_p(\theta - \theta_d) = \tau_{\text{ext}} \quad (2)$$

$$M_d(\ddot{\theta}_d - \ddot{\theta}_0) + B_d(\dot{\theta}_d - \dot{\theta}_0) + K_d(\theta_d - \theta_0) = \tau_{\text{ext}} \quad (3)$$

where k_d and k_p are positive gains, τ_{ext} is the sensed joint torque, θ_0 is the nominal trajectory we wish the system to track, M_d is an effective mass, B_d an effective damping, and K_d an effective spring constant (Lawrence, 1988; Ott et al., 2010). Equation (2) represents the closed-loop dynamics for the manipulator controlled by a joint-level PD control law. The dynamics of the admittance controller in (3) adjust the desired joint angle θ_d that appears in the manipulator's PD controller as a function of the sensed joint torque τ_{ext} . Equation (3) specifies that the dynamics of the desired joint signal are equivalent to a forced spring–mass–damper.

2.4. DMPs

DMPs provide a general method for encoding goal directed behaviors in the attractor dynamics of autonomous nonlinear dynamical systems (Schaal et al., 2000, 2007; Ijspeert et al., 2002, 2013; Hogan and Sternad, 2013). For example,

$$\ddot{r} = a(b(r_0 - r) - \dot{r}) + F(t) + C(\gamma) \quad (4)$$

where r_0 is a nominal set point, a and b control the response of r , $F(t)$ is a (nonlinear) forcing function, and $C(\gamma)$ is a coupling term that depends on the parameters γ , defines a DMP model (Ijspeert et al., 2013). Physically, r in (4) can be used to represent different elements of a given system, such as a set of joint angles or the pose of an end-effector frame. In the case where $F(t) = 0$ and $C(\gamma) = 0$, the dynamics in (4) reduce to a simple linear point attractor and the value of r will stabilize to the set point r_0 . In the more general case, i.e. where $F(t) \neq 0$ and/or $C(\gamma) \neq 0$, a variety of complex behaviors can be encoded in the dynamics of r . Note that allowing $r = \theta_d - \theta_0$, $C(\gamma) = \tau_{\text{ext}}$, and $F(t) = 0$, the dynamics in (4) have the same form as the dynamics of the admittance controller in (3). Admittance controllers are, thus, interpreted as a special case of a DMP in this work.

2.4.1. CPGs. As noted by Ijspeert et al. (2013), CPGs are equivalent to cyclic DMPs. In this work, we define CPGs to be chains of N coupled oscillators where the dynamics of each oscillator are modeled by

$$\dot{\rho}_i = 2\pi v_i + \sum_{j=1}^{N-1} w_j \sin(\rho_j - \rho_i - \phi_{ij}) \quad (5)$$

$$\ddot{r}_i = a_i \left(\frac{a_i}{4} (R_i - r_i) - \dot{r}_i \right) \quad (6)$$

$$x_i = r_i \sin(\rho_i) \quad (7)$$

where (5) is referred to as the canonical system that is integrated to determine the phase of oscillator i , ρ_j is the phase of oscillator j , v_i is an intrinsic frequency, and the weighting terms w_{ij} and phase offset ϕ_{ij} determine the coupled relationship between oscillators i and j (Ijspeert and Crespi, 2007). Equation (6) defines stabilizing dynamics for the amplitude parameter r , where a_i is a positive rate constant, and R_i is the desired amplitude set point. The cyclic function in (7) defines the output of each oscillator.²

3. Shape in compliant control

3.1. Shape functions

Shape functions provide the basis for specifying the kinematic coupling relationships between the motion of individual degrees of freedom in the highly articulated systems considered in this work. More specifically, a shape function h maps a collection of scalar shape parameters $\sigma(t) = (\sigma_1(t), \sigma_2(t), \dots, \sigma_M(t)) \in \Sigma \subset \mathbb{R}^M$, where Σ is the *shape parameter space* that is defined by a time-varying set of shape bases $\beta(t) = (\beta_1(t), \beta_2(t), \dots, \beta_M(t)) \in \mathbb{R}^{N \times M}$, into the N -dimensional joint space, $\theta \in \mathbb{R}^N$, of a given system, i.e. $h : \mathbb{R}^M \times \mathbb{R}^+ \rightarrow \mathbb{R}^N$. We define that each of the individual joints effected by a change in value of a single shape parameter, through its associated shape basis, are kinematically coupled in this work. Similar to modal shape functions (Section 2.1) and kinematic synergies (Section 2.2), this work, in part, considers shape functions that couple the relative motion of collections of a system's internal joints in such a way that the effective dimensionality of the associated configuration space is reduced. In this case, the dimension of the shape space is defined such that $M < N$. However, the upper limit considered in this work is $M = N$, which represents the case where there is no inter-joint coupling.

Take as an example a system where $\theta \in \mathbb{R}^3$, $\Sigma \subset \mathbb{R}^2$, and we have the special case that the shape function is linear in the shape parameters,

$$\theta = h(\sigma(t), t) = \sigma_1(t) \beta_1(t) + \sigma_2(t) \beta_2(t). \quad (8)$$

Furthermore, we define the shape bases in (8) to be time invariant; specifically $\beta_1 = [1, 0, -1]$ and $\beta_2 = [0, 1, 0]$. In this example, we would thus state that joints one and three are kinematically coupled through changes in $\sigma_1(t)$ under β_1 and that joint two is independently controlled by $\sigma_2(t)$.

Note that shape functions are thus very closely related to both kinematic synergies as well as to modal shape functions. The primary differences are that shape functions: (1) explicitly consider both point-to-point and cyclic changes in the values of the parameters $\sigma_i(t)$; (2) allow the basis vectors $\beta_i(t)$ to be time varying; and (3) do not necessarily assume that the shape functions are linear in the shape parameters.

3.2. SBC

Shape functions provide the basis for how a system's internal degrees of freedom are coupled during nominal locomotion. However, un-modeled features, uncertainty, etc., often disturb nominal conditions and a controller is needed to adapt the system's behavior. SBCs are introduced in this work to provide a generalizable framework for deriving controllers that adapt the locomotive behaviors of articulated systems while explicitly preserving the intrinsic coordination specified by different shape functions.

For example, consider the special case

$$\theta = h(\sigma(t)) = \sum_{i=1}^M \sigma_i(t) \beta_i = J\sigma(t) \quad (9)$$

where the columns of J are time-invariant shape bases β_i , which are also assumed to be linearly independent, and $\sigma(t) = [\sigma_1(t), \sigma_2(t), \dots, \sigma_M(t)]^T$. In this case it is possible to map a conventional admittance controller defined in joint space into an equivalent expression defined in shape-parameter space, Σ . Specifically, computing the time derivatives of the shape function h in (9), we find $\dot{\theta} = J\dot{\sigma}$, and $\ddot{\theta} = J\ddot{\sigma}$, which can be substituted into (3),

$$M'_d(\ddot{\sigma}_d - \ddot{\sigma}_0) + B'_d(\dot{\sigma}_d - \dot{\sigma}_0) + K'_d(\sigma_d - \sigma_0) = C(\tau_{\text{ext}}) \quad (10)$$

where $M'_d = J^T M_d J$, $B'_d = J^T B_d J$, $K'_d = J^T K_d J$, $C(\tau_{\text{ext}}) = J^T \tau_{\text{ext}}$, σ_d is a desired shape parameterization, and σ_0 a nominal shape parameterization.³ The expression in (10), thus, defines the dynamics of a *shape-based admittance controller* with external forcing measured by the *shape force* $C(\tau_{\text{ext}})$.

Similarly to (3), Equation (10) takes as input a set of joint torques and produces a set of desired joint positions as output. However, there is an intermediate step in which the joint torques and dynamic response matrices in (3) are explicitly mapped into the shape-parameter dynamics (10). The shape-parameter dynamics are then numerically integrated at each time step during the online implementation of the controller, producing an updated desired shape parameterization σ_d . The desired joint angles (tracked by a low-level position-based controller) are then determined by using the shape function, i.e. $\theta_d = h(\sigma_d, \beta)$.

Note that solving for σ_d by numerically integrating (10) introduces the necessary condition that M'_d be invertible. This is equivalent to the requirement that both M_d be full rank and that the shape bases be linearly independent. While M_d is user specified, and is thus assumed to be full rank, several examples in Section 4 use shape functions whose shape bases are not necessarily linearly independent. In this case, we return to the observation in Section 2 that an admittance controller defined in the joint space is a special case of a DMP with torque-based feedback. We use this observation to define that (10) is a special case of what we refer to as a *shape-based DMP*.

Furthermore, leveraging the generality of DMPs,

$$M_d^\sigma \ddot{\sigma}_d + B_d^\sigma \dot{\sigma}_d + K_d^\sigma (\sigma_d - \sigma_0) = C(\tau_{\text{ext}}) \quad (11)$$

where M_d^σ , B_d^σ , and K_d^σ are assumed *only* to be positive definite, with $C(\tau_{\text{ext}}) = J^T \tau_{\text{ext}}$ and $J = \partial h / \partial \sigma$, also defines a shape-based DMP.⁴ In this case, the desired shape parameters have a similar response to external forces as those in (10), but (11) offers the benefit of relaxing the assumptions on the shape bases. The shape-based DMP in (11) was used as the basis for deriving SBCs in the examples presented in Section 4 and experiments in Sections 5. Note that the gains M_d^σ , B_d^σ , and K_d^σ are, in general, free parameters that need to be defined. In each of the examples and experiments presented in this work the gains were set such that the associated shape dynamics (11) were critically damped.

4. Shape-based compliance in locomotion

We present the results from several examples where SBCs were implemented on the two platforms shown in Figure 1. The first platform was a snake-like robot and the second a walking hexapod. Both robots were assembled using a common set of modular components (Rollinson et al., 2013, 2014b; Ford et al., 2014). Series-elastic actuators served as the active degrees of freedom in each platform. Absolute position encoders on each side of a torsional-elastic spring, located just before the output of each actuator, made it possible to measure the spring deflections and thus output torques of each joint; these measurements were used in the SBCs for both platforms.

The examples presented in this section are provided to demonstrate the basic functionality of SBC as well as to provide context for the practical difference between centralized versus decentralized kinematic coupling in compliant, articulated control. In general, the exact values of different parameters, such as the external forces applied or relative magnitude of the gains (under the assumption that the controller response remains critically damped), could be varied quite significantly without changing the underlying functionality of the controllers presented. More thorough experimental results that evaluate the performance of SBCs under different environmental conditions are presented in Section 5.

In addition, each of the examples (except that shown in Figure 8b) considers a static scene wherein the robots are not locomoting; the examples are meant to clearly demonstrate how SBCs with different levels of coupling react to *isolated* external forces. To lend better insight into the performance of the SBCs while the robots are moving through different environments, using the shape functions presented in this section, we note that the behavior of the controllers are entirely independent of the phase of the underlying shape functions. More specifically, *the controllers function by regulating the systems' shape changes around nominal shape patterns* (specified by the shape functions). Whether the nominal shape patterns are changing (i.e. when the phase is varied) or are held fixed (as in the examples presented in this section) the SBCs' basic functionality will remain exactly the same. Extension 1 presents several

examples that demonstrate the performance of SBCs while the phases of different shape functions are continuously varied.

4.1. Whole-body coupling

4.1.1. Snake-like robot. In each of the examples for the snake-like robot presented in this work, the shape functions are defined in terms of the planar serpenoid model originally developed by Hirose (1987),

$$\theta = A \sin(\eta s - \omega t) \quad (12)$$

where A is an amplitude parameter, η is the spatial frequency that determines the number of waves formed by the robot's body, ω is the temporal frequency that determines how fast waves travel down the body, and s is the arc length measured from the head of the robot. For the discrete-bodied snake-like robot in Figure 1, $s = \{0, \delta s, 2 \cdot \delta s, \dots, N \cdot \delta s\}$, where δs is the link length and $N = 18$. Note that the axes of rotation of adjacent joints are rotated by 90° with respect to the centerline of the mechanism. As a result, there are only $N' = 9$ co-planar joints in the system, i.e. only half the system's joints are controlled in each of the planar examples presented in this section.

The serpenoid model in (12) can be rewritten in the form of a shape function,

$$\begin{aligned} \theta &= h(\sigma) = A(t) \cos(\omega t) \sin(\eta s) - A(t) \sin(\omega t) \cos(\eta s) \\ &= \sum_i^2 \sigma_i(t) \beta_i \end{aligned} \quad (13)$$

where the shape parameters are $\sigma_1(t) = A(t) \cos(\omega t)$ and $\sigma_2(t) = -A(t) \sin(\omega t)$, and the shape bases are $\beta_1 = \sin(\eta s)$ and $\beta_2 = \cos(\eta s)$.⁵ We define that there is *whole-body* or *global coupling* between each of the N' co-planar joints under both β_1 and β_2 in (13); a change in either $\sigma_1(t)$ or $\sigma_2(t)$ will effect a change in value of all N' joints (Travers and Choset, 2015).

The dynamics of the SBC for the shape function in (13) are expressed in the form (11) for this example,⁶ where $\sigma(t) = (\sigma_1(t), \sigma_2(t))$ and $J = \partial h / \partial \sigma = [\beta_1, \beta_2]$. However, the fact that the shape parameters share both an amplitude and frequency parameter allows us to *reduce* the shape dynamics. Specifically, we use the fact that $\sigma = [\cos(\omega t), -\sin(\omega t)]^T A(t) = J^A A(t)$ to rewrite (11) in terms of the dynamics associated with $A(t)$ directly,

$$M_d^A \ddot{A}_d + B_d^A \dot{A}_d + K_d^A (A_d - A_0) = C^A(\tau_{\text{ext}}) \quad (14)$$

where $M_d^A = (J^A)^T M_d^\sigma J^A$, $B_d^A = (J^A)^T B_d^\sigma J^A + 2(J^A)^T M_d^\sigma \dot{J}^A$, $K_d^A = (J^A)^T K_d^\sigma J^A + (J^A)^T B_d^\sigma \dot{J}^A + (J^A)^T M_d^\sigma \ddot{J}^A$, and $C^A(\tau_{\text{ext}}) = J^A J \tau_{\text{ext}}$. Note that we assume M_d^σ is positive definite and, thus, M_d^A is positive by definition, i.e. (14) can always be solved for A_d .

Figure 2 shows the results of implementing the SBC defined by (14) on the snake-like robot. In this example

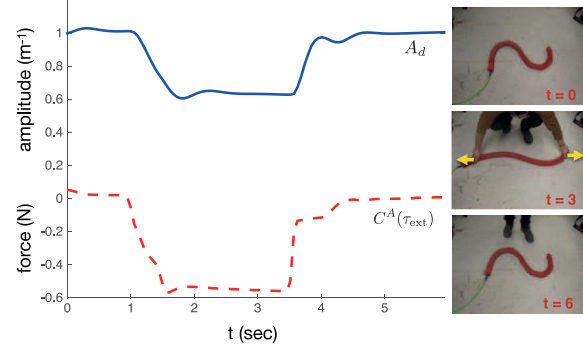


Fig. 2. Example of the whole-body coupled SBC implemented on the snake-like robot. A single-amplitude parameter of the static waveform shown is compliantly controlled in response to the external forces applied.

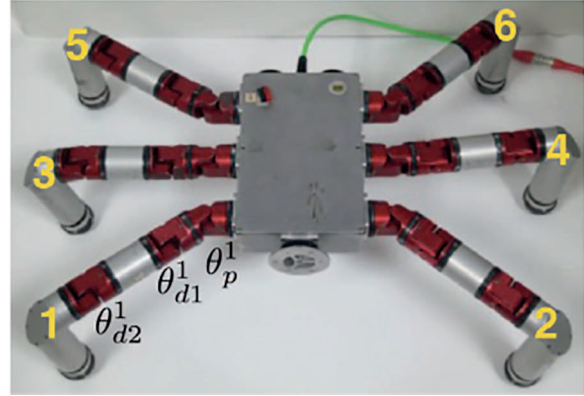


Fig. 3. Modular hexapod robot.

$\omega = 0$, i.e. the wave on the robot's body was stationary, $A_0 = 1$, and $A_d(0) = A_0$. The plot on the left-hand side of Figure 2 shows that at $t = 0$ no external force was measured by the robot, i.e. the corresponding shape force was approximately zero. At $t = 1$ an external force was applied to the robot's body, creating a negative shape force and subsequently causing the value of A_d to decrease. Note that due to the whole-body coupling defined by the shape bases in (13), the amplitude simultaneously decreases over the robot's entire body. At $t = 3.5$ the external force was removed, causing the shape force to return to approximately zero, and thus driving the desired amplitude parameter back to $A_0 = 1$. Note that the controller implemented in the example shown in Figure 2 is the static counterpart to the "single-amplitude" SBC included in the experiments in Section 5.

Note also that the dynamics in (14) define a reduced shape-based DMP that bears a strong resemblance to the oscillator amplitude dynamics in the CPG model in (6). More specifically, rearranging (14) and defining a constant

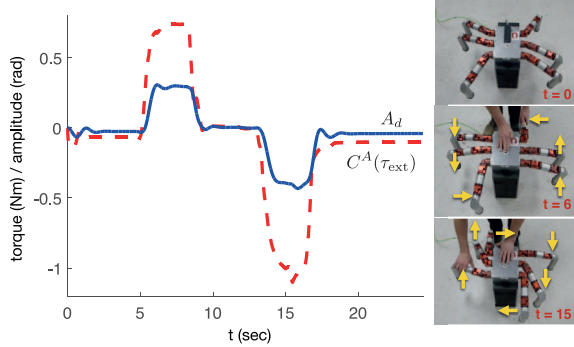


Fig. 4. Example of the whole-body coupled SBC implemented on the hexapod robot. A single parameter controls the offset of each leg in response to the external forces applied.

temporal frequency parameter ν ,

$$\begin{aligned} \dot{\rho} &= 2\pi\nu \\ \ddot{A}_d &= (M_d^A)^{-1} (C^A(\tau_{ext}) - B_d^A \dot{A}_d - K_d^A (A_d - A_0)) \\ \theta &= A_d \sin(\eta s - \rho) \end{aligned}$$

provides an interpretation of the whole-body coupled SBC; it defines a single oscillator whose time-varying amplitude dynamics are a function of torque feedback (see (5)–(7)).

4.1.2. Hexapod robot. The shape functions used to define SBCs for the hexapod robot shown in Figure 1 make the assumption that, when the robot is walking, it continuously executes an alternating tripod gait. More specifically, each leg of the robot has three joints; a proximal joint, θ_p^i , that rotates about a body-fixed yaw axis, and two distal joints, θ_{d1}^i and θ_{d2}^i , that rotate about body-fixed pitch axes (see Figure 3). The individual joint trajectories for leg i are defined by

$$\theta_p^i = A_i(t) + c_1 \cos(\omega \cdot t - \phi) \quad (15)$$

$$\theta_{d1}^i = c_2 \sin(\omega \cdot t - \phi) / (1 + \exp(-c_3 \sin(\omega \cdot t - \phi))) \quad (16)$$

$$\theta_{d2}^i = -c_2 \sin(\omega \cdot t - \phi) / (1 + \exp(-c_3 \sin(\omega \cdot t - \phi))) \quad (17)$$

where $i \in \{1, 2, \dots, 6\}$, c_1 , c_2 , and c_3 are constants that determine the stride length, maximum height of each foot during flight, and shape of the foot trajectory (during flight), respectively. The amplitude parameter $A(t)$ in (15) controls the offset position around which the proximal joint in each leg oscillates. The trajectories of the two distal joints, (16) and (17), have sigmoidal “activation windows” that lift the feet with sinusoidal trajectories for one half of the gait cycle and set the joint values equal to zero in the other half of the cycle, i.e. during stance. The phase parameter ϕ is set to zero for legs 1, 4, and 5 and is equal to π for legs 2, 3, and 6, i.e. the three legs in each support tripod are π radians out of phase relative to the legs in the opposing tripod.

Shape functions for the hexapod are represented by $\theta = h(\sigma) = (\theta_p^1, \theta_{d1}^1, \theta_{d2}^1, \dots, \theta_p^6, \theta_{d1}^6, \theta_{d2}^6) \in \mathbb{R}^{18}$, i.e. the sequential list of the joint angles in each leg. We define the shape parameters in terms of different combinations of the proximal-joint offsets $A_i(t)$ that appear in the trajectories (15) for each leg. More specifically, the shape functions can be simplified to

$$\theta = h(\sigma, \beta, t) = \sum_i^M \sigma_i(t) \beta_i + f(t) \quad (18)$$

where the function $f(t)$ represents the joint trajectories that coordinate the alternating tripod gait under nominal conditions, the shape parameters are $\sigma_i(t) = A_i(t)$, and the shape bases $\beta_i \in \mathbb{R}^{18}$ contain zeros in the 12 rows that correspond to the distal joints in the system; the number of shape bases M and position of non-zero entries in the six rows of the β_i that correspond to the proximal joints in θ (i.e. $\{\beta(1), \beta(4), \dots, \beta(16)\}$) determine the kinematic coupling in the hexapod shape functions. For example, in the case where $M = 1$ and we assume that β has six non-zero entries, we define that the system is whole-body coupled; changing the value of σ will effect the offset of each leg.

Figure 4 shows the result of implementing the whole-body coupled SBC on the hexapod robot while it was suspended above the ground, the frequency ω of the alternating tripod gait was set to zero (see (15)–(17)), and J in (11) was defined by $J = \beta$. During the example, an external force was first locally applied in the positive direction to leg 1. Note that the offsets of all six legs were rotated in the positive direction about a body-fixed axis pointing vertically up in response. At time $t = 6$ a force was applied to leg 6 in the opposite direction, creating a negative shape force that caused the offsets of all six proximal joints to rotate in the negative direction with respect to the body-fixed frame.⁷

4.2. Decentralized coupling

This work assumes that SBCs with whole-body coupling are centralized control methods in the sense that forces applied locally to a robot’s body will affect global changes in its shape. The experimental results that are presented in Section 5 demonstrate that this type of global change in shape works best in regularized environments. However, in complex terrains, the global shape that is preserved by centralized SBCs may not be compatible with the local environmental features. More specifically, the body shapes necessary to locally comply to irregular features in unstructured terrains may be outside the span of the shape bases defined in the fully coupled shape functions. In this case, this work supports the belief that a higher degree of decentralization in the SBCs, in which fewer individual degrees of freedom are kinematically coupled, may be necessary to enable robots to locomote effectively.

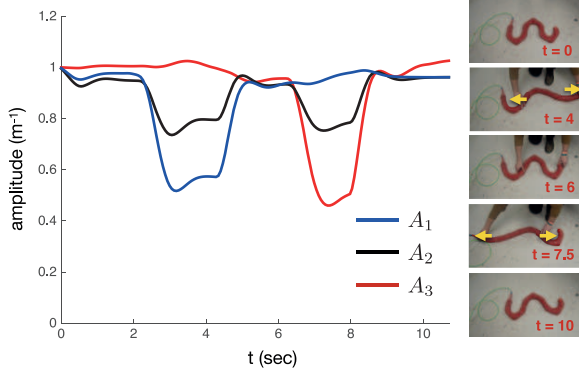


Fig. 5. Example of decoupled SBC implemented on the snake-like robot. There are three separate “windows” in which the amplitude of the waveform shown is independently controlled in response to external forcing.

4.2.1. *Snake-like robot.* Previous work by Travers et al. (2016) introduced Gaussian-shaped spatial activation windows as the mechanism for kinematically coupling different collections of adjacent joints along a snake-like robot’s body. For example, consider the shape function

$$\theta = A(s, t) \sin(\eta s - \omega t) \quad (19)$$

where

$$A(s, t) = \sum_{j=1}^W A_j \exp\left(-\frac{(s - \mu_j(t))^2}{2\psi^2}\right) \quad (20)$$

where W is the number of spatial activation windows, A_j is the amplitude in window j , ψ defines the width of the window (as a function of arc length), and each μ_j defines the location of the center of a window. The shape function in (19) makes it possible to modulate the amplitude of the wave $\sin(\eta s - \omega t)$ in W individual windows spatially distributed along the robot’s body.

In the examples presented in this work, the locations (determined by $\mu_j(t)$) and extents (determined by ψ) of each spatial activation window were specified such that neighboring windows had minimal overlap, i.e., the amplitude in one window had little effect on the joints in the adjacent windows. The spatial activation windows thus made it possible to independently couple the amplitude of different groups of joints along the robot’s body. Therefore, the total number and spatial extent of each window was used to determine the *level of kinematic coupling* specified by each shape functions for the snake-like robot in the form (19).

For example, Figure 5 shows the result of implementing the SBC for the shape function (19) with three spatial activation windows. The window centers were selected to be at the points of highest curvature of the waveform shown at $t = 0$. Each window covered approximately one third of the robot’s arc length. The waveform was specified such that the robot’s body formed 1.5 total waves, and the temporal phase parameter ω was set to zero. Similarly to Section

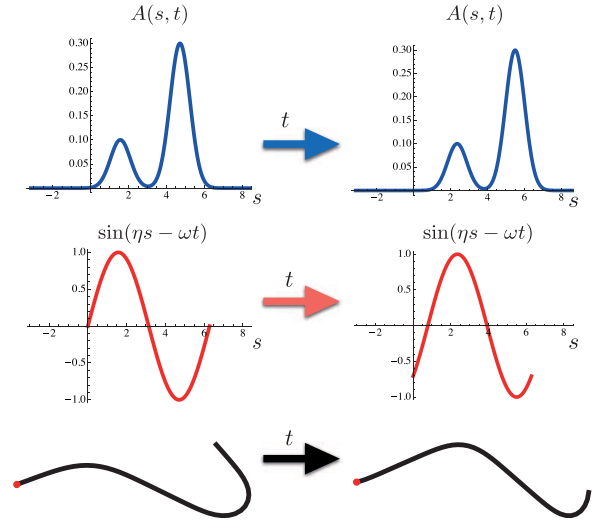


Fig. 6. Spatially propagating amplitude information with the serpenoid wave using two moving windows. The plots in the top row display an amplitude signal as a function of arc length at two different times. The amplitude signals modulate the waves shown in the middle row to produce the shapes of the robot shown in the bottom row.

4.1.1, the SBC dynamics in the form (11) were reduced to a set of amplitude parameters (A_1, A_2, A_3) in this example, where $C(\tau_{\text{ext}})$ was defined in terms of

$$J = \begin{bmatrix} \exp\left(-\frac{(s - \mu_1)^2}{2\psi^2}\right) \sin(\eta \cdot s), \exp\left(-\frac{(s - \mu_2)^2}{2\psi^2}\right) \sin(\eta \cdot s), \exp\left(-\frac{(s - \mu_3)^2}{2\psi^2}\right) \sin(\eta \cdot s) \end{bmatrix}^T \quad (21)$$

Note that J in (21) has the effect of mapping only the joint torques in the region of the robot’s body covered by each of the spatial activation windows into the corresponding amplitude dynamics (each of which have a form equivalent to (14)). Figure 5 shows that as a result, forces applied locally to different portions of the robot’s body effected only the values of the local amplitude parameters.⁸

The choice to place the window center locations at the points of highest curvature on the serpenoid waveform in the example shown in Figure 5 was not unique. Effectively any sequential combination of joints can be coupled by different choices of the spatial activation window parameters in (20). Furthermore, the value of the window center locations are defined to be functions of time in (20). This design decision was made due to the fact that we observed, in examples where ω in (19) was not assumed to be zero, defining the window center locations $\mu_j(t)$ to travel down the robot’s body at the same rate as the serpenoid waveform (i.e. $\mu_j(t) = \mu_j^0 + \omega/\eta t$, where μ_j^0 is the initial location of the spatial activation window)⁹ provided an intuitive means of “passing shapes” down the system’s body (see Figure 6). We present evidence in Section 5 that suggests there

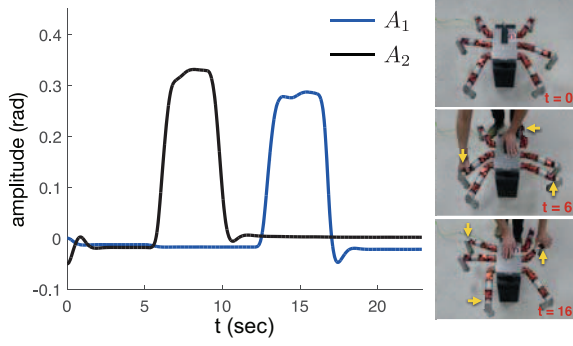


Fig. 7. Example of decoupled SBC implemented on the hexapod robot. The phase offset of only three legs at any one time are coupled and controlled in response to the external forces applied.

are measurable benefits to spatially propagating amplitude information with the serpenoid carrier wave using the moving windows. Note that as a result of implementing the moving windows, the shape bases for the decoupled serpenoid shape functions become *time-varying*. However, this does not fundamentally effect the implementation of the resultant SBCs; the shape forces are still defined by $C(\tau_{\text{ext}}) = \partial h / \partial \sigma$ and, while the specific joints in each spatial activation window will change as a function of time, the *total number of joints* in each window, and thus the extent of kinematic coupling, will remain fixed.

4.2.2. Hexapod robot. Changing the coupling relationship between the proximal-joint offset parameters in the hexapod shape functions (18) is straightforward; the total number of shape bases M , and non-zero entries in each β_i determine the relative level of kinematic coupling. For example, Figure 7 shows the results of implementing the SBC associated with a shape function defined by two shape bases that kinematically coupled the three legs in the system’s opposing support tripods (i.e. legs 1, 4, and 5 and legs 2, 3, and 6). The shape parameters associated with the shape bases, $\sigma = (A_1, A_2)$, corresponded to the proximal-joint offsets for each tripod.

Similarly to the example in Figure 4, the robot shown in Figure 7 was suspended above the ground and the frequency ω of the alternating tripod gait was set to zero. In this example, an external force was first applied to leg 3 (which is in tripod 2) at $t = 6$, causing a positive shape force to act on the A_2 shape dynamics. The pictures on the right-hand side of Figure 7 show that as a result, the proximal-joint offsets in the legs in tripod 2 were increased, causing the legs to rotate in the positive direction (with respect to the body fixed frame). Similarly, when a force was applied in the positive direction to leg 4, each of the proximal-joint offsets in the legs in tripod 1 were correspondingly increased.

4.3. Three-dimensional coupling

We present several examples of shape functions and their corresponding SBCs that make it possible to coordinate

non-planar shape changes. We believe that these types of somewhat more complicated motions will be crucial in extending the future autonomous capabilities of articulated locomotion systems operating in highly unstructured terrains.

4.3.1. Snake-like robot. We mentioned in Section 4.1 that the rotational axes of adjacent joints in the snake-like robot are rotated by ninety degrees relative to the center line of the mechanism. In general, this allows the system to take on three-dimensional shapes. As a specific example, consider

$$\theta^o = \sum_{k=1}^W A_k \cos(\varphi_k) \exp\left(\frac{-(s - \mu_k(t))^2}{2\psi^2}\right) \sin(\eta s - \omega t) \quad (22)$$

$$\theta^e = \sum_{k=1}^W A_k \sin(\varphi_k) \exp\left(\frac{-(s - \mu_k(t))^2}{2\psi^2}\right) \sin(\eta s - \omega t) \quad (23)$$

where (22) is used to coordinate the system’s *odd* joints and (23) the *even* joints. Spatial activation windows that locally modify the amplitude of a serpenoid waveform (analogously to (19)) are included in both (22) and (23). Additionally, sinusoidal functions that act on the rotational parameters φ_k are also included in both (22) and (23).

To physically interpret (22) and (23), assume first that the spatial frequency η is set such that the robot’s body forms a single wave, the temporal frequency is set such that $\omega = 0$, and a single activation window covers the robot’s entire body, i.e. the amplitude of the serpenoid wave is constant. Assume also that φ_1 is originally equal to zero. In this case, the values of each of the even joints will be equal to zero and the serpenoid waveform $A_1 \sin(\eta s)$ will be entirely contained in a plane normal to the rotational axes of the odd joints. Assume now that the value of φ_1 is gradually increased until it reaches a value of $\pi/2$. When $\varphi_1 = \pi/2$, the values of all of the odd joints will equal to zero and the serpenoid waveform will be entirely contained in a plane normal to the rotation axis of the even joints. Thus, in this example, incrementally varying φ_1 gradually *rotates* the serpenoid waveform from one body plane to the other. More generally, in examples where $W \neq 1$, Equations (22) and (23) make it possible to *locally* rotate different portions of the serpenoid waveform between body planes.

For example, Figure 8a shows the result of implementing the SBC associated with the shape function $h(\sigma(t), t) = (\theta^o, \theta^e)$. Three spatial activation windows, that each covered approximately one third of the robot’s body, were defined in this example. The spatial frequency η was set such the robot’s body formed 1.5 waves, the temporal frequency was set such that $\omega = 0$, and the amplitude parameters were set to $A_k = 1$, where $k = \{1, 2, 3\}$. The shape parameters were defined in terms of the rotational parameters $\sigma = (\varphi_1, \varphi_2, \varphi_3)$ and, thus, the shape forces in terms of $J = [\partial h / \partial \varphi_1, \partial h / \partial \varphi_2, \partial h / \partial \varphi_3]$. Note that, in

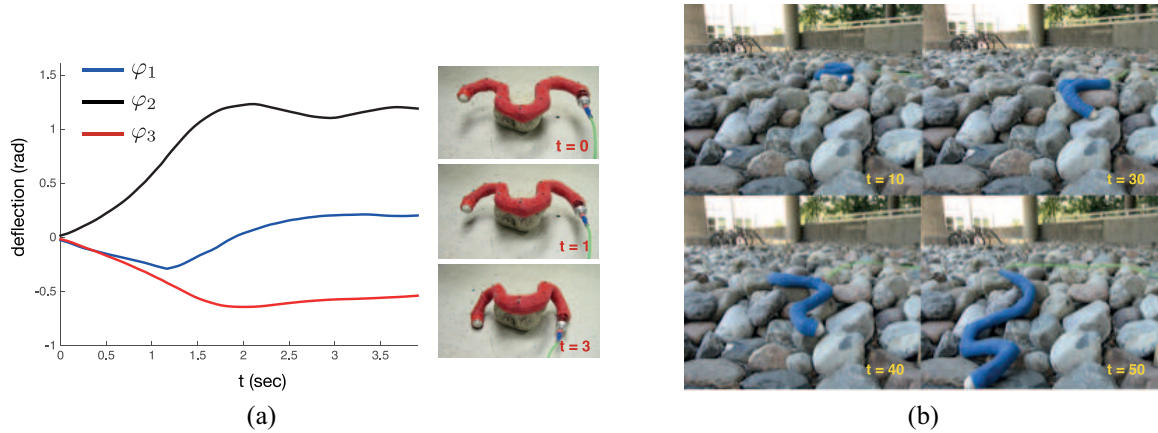


Fig. 8. Examples of applying the torsional SBC to the snake-like robot (a) while perched on a rock and (b) while moving through a pile of rocks outside. (a) Torsional compliance with three spatial activation windows. The robot here adapts its shape to three-dimensional objects by “rotating curvature” from one body plane to another. (b) Snake-like robot autonomously traversing three-dimensional pile of rocks using torsional compliance SBC. Extension 1 shows this sequence in realtime, and helps highlight the effect that partially decentralized, three-dimensional shape control has on locomotion control.

this example, the shape functions have a *nonlinear dependency* on the shape parameters. However, similarly to defining time-varying shape bases, the nonlinear relationship between the shape parameters and shape function does not fundamentally effect the performance of the SBC.

Figure 8a shows that the robot in this example was originally placed in a position at $t = 0$ where the front and back of its body were suspended above the ground, while the middle portion of its body was supported by an obstacle. The pictures in Figure 8a also show that as the trial began, the “rotationally compliant” SBC enabled the system to adapt its shape to the three-dimensional obstacle using the force of gravity acting on the suspended portions of its body.

Figure 8b shows the result of implementing the same SBC as that used in the example shown in Figure 8a. However, in this example the robot was placed on an unstructured pile of rocks and the temporal frequency was non-zero ($\omega = 1$). Figure 8b shows what to the best of the authors’ knowledge is the first autonomous trial of a snake-like robot adapting its shape to highly unstructured three-dimensional clutter to produce effective forward locomotion.

4.3.2. Hexapod robot. The individual leg trajectories in (15)–(17) used to define the alternating tripod gait function $f(t)$ in (18), contain the parameters c_1 , c_2 , and c_3 that determine the “shape” of the gait. Assuming the phase ωt for each leg is held constant at $\pi/2$, and that the proximal joint offsets are set to zero, the joint angles for each leg are reduced to $\theta_{i_j} = c_2^j [0, 1, -1]^T$. In this case, the parameter c_2 governs the height of each foot relative to the body (see Figure 9). Furthermore, we can group the joint angles from each leg to define a shape function $\theta = h(\sigma, \beta) = \sum_{i=1}^M \sigma_i \beta_i$, where $\sigma = (c_2^1, c_2^2, \dots, c_2^6)$ and the shape bases

$\beta_i \in \mathbb{R}^{18}$ determine the inter-leg coupling similarly to the β_i in (18).

Figure 9 shows the result of implementing the SBC associated with the “leg-height” shape function, where the three legs on each side of the robot’s body were coupled. Note that the definition of the shape force in (11) had to be modified in this example to account for the fact that during nominal stance the two distal joints in each leg measured a non-zero torque due to gravity. More specifically, the shape force in the SBC for the example shown in Figure 9 was defined by $C(\tau_{\text{ext}}) = F_g + J^T \tau_{\text{ext}}$, where $F_g = -J^T \tau_g$ and τ_g was the expected quasi-static torque due to gravity. The results in Figure 9 show that the SBC in this example adjusted the foot heights of each leg in response to a force applied to the feet on the left-hand side of the robot’s body; the force was applied by lifting the platform the robot was standing on at $t = 0$. Adjusting the individual foot heights relative to the robot’s body had the net effect of adjusting the system’s pose to comply to the externally applied forces.

5. Experiments

The primary objective of this work was to investigate the role that kinematic coupling plays in the compliant locomotion control of highly articulated systems. The SBC framework presented in Section 3 and applied to several examples for the snake-like and hexapod robots in Section 4 provided the basis for this investigation. This section presents experimental results that compare the performance of the snake-like and hexapod robots moving through different terrains executing SBCs derived from a variety of shape functions. Specifically, the shape functions were designed to incrementally vary the relative-level of kinematic coupling between the systems’ internal joints in the associated

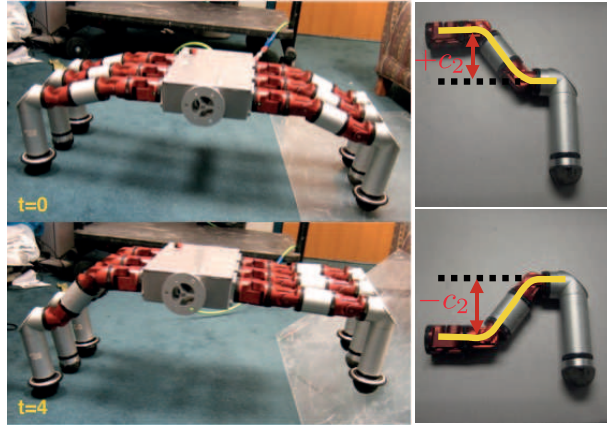


Fig. 9. Three-dimensional “leg-height compliance.” Instead of controlling leg offset, the SBC in this example compliantly adjusts the leg-height parameter c_2^i .

SBCs. The environments were selected such that they were varied in their relative level of underlying regularity.

In each of the experiments for both robots, the dynamic response of the shape parameters was set to be critically damped, as discussed in Section 3. However, the magnitude of the response, and thus total extent to which the “shape” of the robot changes in response to external forcing was very much dependent on the relative value of the gain parameters M_d^σ , B_d^σ , and K_d^σ in comparison with the value of $C(\tau_{\text{ext}})$ in (11). More specifically, manually adjusting the gains made it possible to specify *how compliant* a particular shape parameter was in response to a fixed external force. In practice, we found that shape dynamics that were either *too compliant* or *too stiff* both produced very different, but poor overall performance in terms of the metric discussed below. The shape gains were, thus, hand tuned to lie between the empirically determined “too compliant” and “too stiff” limits for each robot. Once set, however, the gains were held fixed throughout the experimental procedures. Gain adjustment is discussed further in Section 6.

5.1. Snake-like robot

The experimental testbed used to compare the performance of the snake-like robot executing different SBCs consisted of a rearrangeable peg board and a four-camera OptiTrack motion capture system (NaturalPoint Inc.). The robot used in the experiments had 18 joints (i.e. $N = 18$) joints total, but only the 9 co-planar joints were actively controlled (i.e. $N' = 9$). The robot was placed in a braided polyester sleeve attached to a plastic cap at the head of the system; the sleeve and cap helped to reduce the friction between the robot and the pegs. Nine reflective markers were attached to the sleeve along the robot’s backbone and were used to accurately measure the position of the system during each trial.

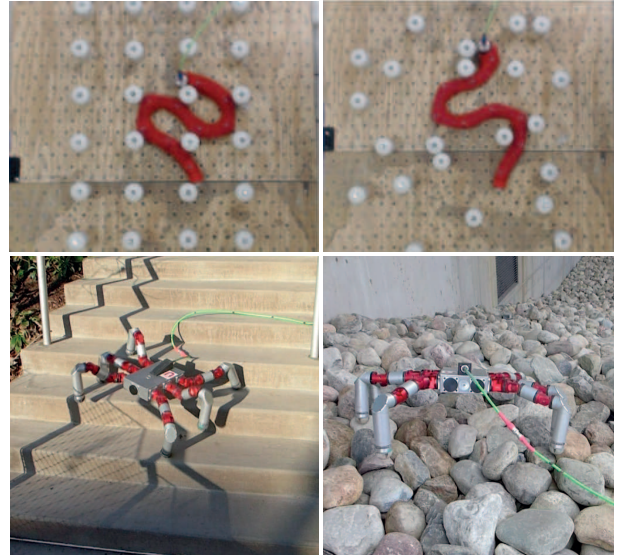


Fig. 10. Snake-like and hexapod robots in the structured (regularized peg array and concrete steps) and unstructured (randomized peg array and sloped rock pile) terrains used to conduct experiments in this work.

Two different peg arrays were used for the snake-like robot experiments. The first was the highly structured, regularized array and the second an unstructured, randomized array (both arrays are shown in Figure 10). In each experiment, the shape functions used to derive the SBCs were defined using (19) with normalized wave parameters $\eta = 1.5$ and $\omega = 1$. The number of spatial activation windows in each shape function was varied across the sets of trials in both experiments. In the lower limit, a single activation window was used to define a whole-body coupled, fully centralized SBC. In the upper limit, nine activation windows, that approximately covered a single joint each, were used to derive a fully decentralized SBC. Several shape functions and their associated SBCs that fell between these two limits were also evaluated. Specifically, SBCs defined by shape functions with three and six activation windows, that each approximately covered one third and one sixth of the robot’s body, respectively, were included in the experiments as well.

The final controller that was included in the experimental comparisons was what we refer to as a “CPG with force” controller. For this controller, we assumed that each joint in the robot had its own oscillator, but that the individual oscillators were phase locked. The amplitude dynamics in the CPG oscillator model in (6) were modified to include a shape force equivalent to that used in the “nine-window” fully decentralized SBC. The only difference between the nine window SBC and the CPG with force controller was that the SBC spatially propagated amplitude information using the moving windows as discussed in Section 4.2.1. The amplitude parameters in the CPG controller were completely independent.

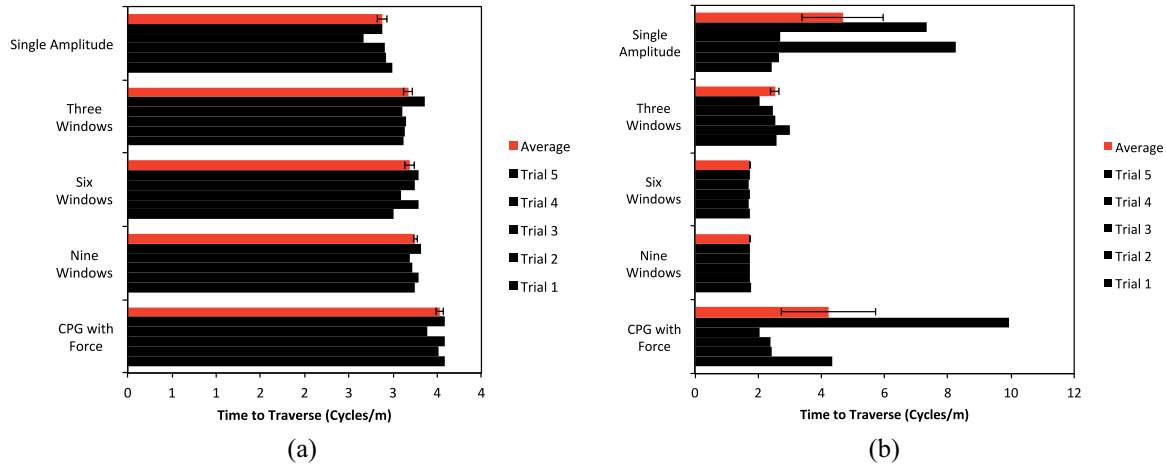


Fig. 11. Experimental results from the two snake-like robot experiments. (a) results of the experiment in the regularized peg array; (b) results of the experiment in the randomized peg array. The results show that there is a slight benefit when using the “single-amplitude” SBC in the regularized peg array, whereas there is a large benefit when using the “nine-window” decentralized controller in the unstructured array.

We note here briefly that a variety of pre-existing controllers for snake-like robots have previously been designed to address navigation through cluttered terrains in general, and peg arrays in particular. Of particular note is the obstacle-aided controller presented by Liljeback et al. (2011); the gait-based compliance controller presented by Rollinson and Choset (2013); the adaptive controllers based on curvature derivatives presented by Date and Takita (2007); the related work on decentralized scaffolding-based locomotion presented by Kano and Ishiguro (2013); the planar method that adapting body shapes based on contact sensors presented by Kamegawa et al. (2012); and the purely torque-based control strategies presented by Rollinson et al. (2014a). A thorough review of related controllers for snake-like robots are presented in the review by Transteth et al. (2009). While a comparison between existing control methods for snake-like robots and the SBCs presented in this work is of interest in general, it is outside the intended scope of this work, i.e. investigating the relative benefits of different levels of coordination in the locomotion control of *different* platforms.

The experiments for the snake-like robot consisted of five individual trials for each controller. The SBC dynamic constants were fixed across each trial (i.e. M_d , B_d , and K_d in (11)). The robot’s performance was measured by dividing the number of times the nominal wave defined by $\sin(\eta \cdot s - \omega \cdot t)$ was propagated from the robot’s head to its tail by the total distance traveled during each trial (measured in terms of the integral of the path length of the system’s center of geometry in meters). This value effectively provided a measure of how many “gait cycles” it took for the robot to travel one meter. Thus, trials that resulted in the robot thrashing in place, or otherwise failing to make forward progress through the peg arrays had higher values (and, thus, lower performance) than trials where the

robot moved smoothly through the pegs. The average performance over the five trials for each controller are shown in red. The variances across the trials are also shown.

Figure 11a shows that in the regularized peg array the performance between the controllers was very close. Each trial throughout the entire experiment resulted in the robot successfully weaving its way through the pegs with very little variation. As expected, the highly coupled shape-preserving structure provided by the single-window shape function enabled the associated SBC to do slightly better, in terms of the time taken to traverse the peg array, than the decentralized SBCs as well as the modified CPG.

Figure 11b shows that the performance between the different controllers was much more varied in the randomized peg array. In particular, the decentralized SBCs did much better in terms of both the time taken to traverse the peg array as well as in how consistent they were in comparison to the fully coupled single-window SBC. This was also expected, as we had hypothesized that the ability of the decentralized controllers to locally adapt the shape of the robot to random environmental features would enable the system to better weave its way through unstructured terrains. Interestingly, the CPG with force controller did measurably worse, in terms of both the average time to traverse the array and variance, than each of the three SBCs with control decentralization. This observation suggests that there appears to be distinct benefits related to spatially propagating amplitude information down the robot in the random peg array.

5.2. Hexapod robot

The experiments for the hexapod robot were conducted on the steps and sloped rock pile both shown in Figure 10. Four different SBCs were derived using shape functions in the

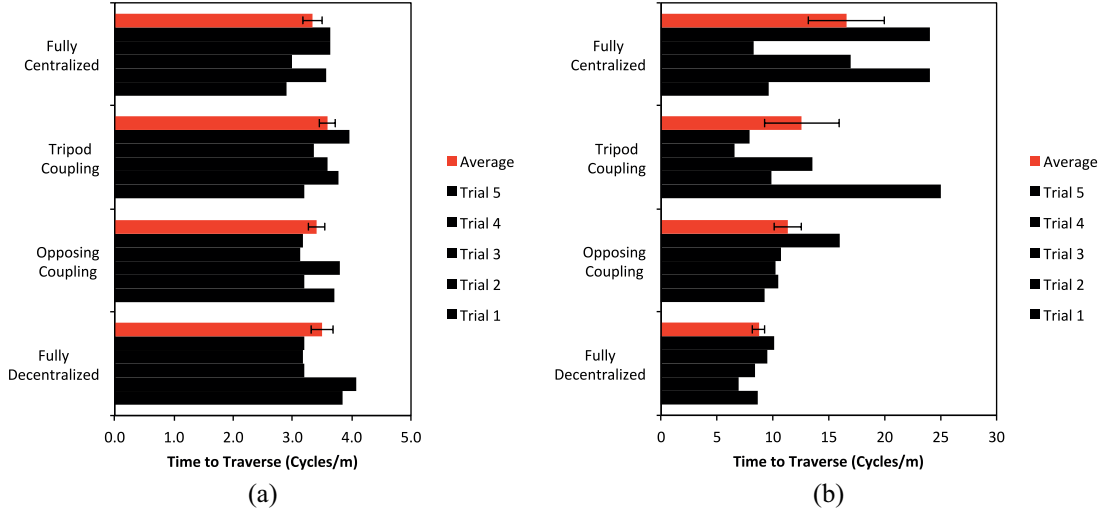


Fig. 12. Experimental results from the two hexapod robot experiments. (a) results of the experiment for walking down stairs; (b) results of the experiment for walking down the rock pile. The results show that there is no meaningful benefit between using a centralized or decentralized controller on the stairs, whereas there is a measurable benefit when using the fully decentralized controller on the rocks.

form (18). The first SBC fully coupled the proximal-joint offsets of all six legs (i.e. identically to the controller used in Figure 4). The second coupled the offsets of the two sets of three legs in each of the opposing support tripods (i.e. identically to the controller used in Figure 7). The third SBC coupled the three sets of two opposing legs on each side of the robot’s body (i.e. legs 1 and 2, 3 and 4, and 5 and 6). The final SBC controlled the proximal-joint offsets of each leg independently. Note that an equivalent to the CPG with force controller was not defined for the hexapod as there was no means to directly propagate amplitude information in the hexapod SBCs.

Five trials for each of the four controllers were conducted in both hexapod experiments. For each of the trials on the steps, the robot was placed on the same initial step in approximately the same position. Each trial was timed, beginning at the point when the robot started moving and ended when the first of its front feet hit the ground at the bottom of the steps. The robot successfully completed each trial in the experiment. The results in Figure 12a show that, similarly to the snake-like robot experiment in the regularized peg array, each of the SBCs had similar performance in terms of the time it took to traverse the steps as well as in consistency (the same cycles/meter performance measure used to evaluate the snake-like robot was also used to evaluate the hexapod). The fully coupled SBC did slightly better than the other controllers in terms of speed, but not significantly. In general, it was much more difficult to make accurate measurements for the hexapod than it was for the snake-like robot (as a motion capture system was not available). Small differences in performance were thus more difficult to detect.

The hexapod experiment on the rock pile also conducted five trials for each of the four SBCs. At the beginning of each trial the robot was placed in approximately the same

initial position at the top of the slope. Each trial was allowed to run for 40 s. The robot’s final position was measured using a tape measure that stretched from the initial position of the robot’s back feet to the location of the foot furthest upslope (i.e. closest to the initial position of the robot) at the end of each trial. The results in Figure 12b show that the robot performed best in terms of both its average speed as well as in consistency using the fully decentralized SBC. The results also show that the SBCs with tripod and opposing leg coupling had similar performance in terms of their average speed, but that the more decentralized controller with opposing leg coupling was more consistent. The fully centralized controller did measurably worse than each of the other SBCs. Thus, a similar trend to that observed in the snake-like robot experiments also emerged for the hexapod: SBCs with higher levels of decentralization performed measurably better as the irregularity of the environment was increased.

6. Conclusion and future work

This work has proposed the idea that the level of coordination in the locomotion control of highly articulated systems is a parameter that can be varied to affect different benefits in different terrains. We showed how shape functions were used to specify different levels of coordination through kinematic coupling relationships. The coupling relationships, in turn, provided the basis for defining the resultant degree of controller centralization in compliant SBCs. Initial experimental evidence was presented that showed there are benefits in using SBCs with different degrees of decentralization in environments with different levels of underlying regularity. Specifically, we found that a greater degree of decentralization worked well across different environmental conditions and was measurably beneficial in unstructured

terrains, whereas centralized SBCs offered slight performance benefits in structured terrains. Two separate platforms were employed in this work to support the generality of our approach and results.

There are, however, several components related to shape functions and SBCs that were not addressed in this work, but that are the focus of ongoing and future work. The first, as discussed in Section 2.2, addresses how shape functions are derived. In each of the examples presented in this work, the shape functions were highly system-specific and user-defined. A natural question with respect to the broader applicability of the shape-based framework is thus whether or not the derivation of shape functions can be automated? As discussed in Section 3.2, once a suitable shape function is defined, the process for deriving a controller that acts directly on the shape parameters is relatively straightforward. Deriving shape functions is thus a necessary condition for making the SBC framework, in its current form, available to arbitrary robot architectures. In our future work, we thus plan to derive shape functions for arbitrary systems using a data-driven approach that is similar in concept to that in Hauser et al. (2007, 2011). However, our planned approach will focus on a broad simulation-based framework where different platforms and a variety of environmental conditions will be used to generate large amounts of motion data. The data will be segmented into similar motion patterns and assessed for quality. A combination of linear and nonlinear dimensionality reduction techniques will then be applied to the resulting data to derive, where possible, low-dimensional representations of families of associated motions. Our objective is to use the resulting expressions to define different classes of shape functions.

This work additionally made the assumption that each of the environments the robots' were deployed in during testing and experimentation were homogenous in the sense that they were either structured or unstructured, but not a combination thereof. For the purpose of evaluating how the level of coupling affected performance in different conditions, the homogenous terrains were sufficient. However, in the future we want to autonomously deploy highly articulated systems in complex environments that contain a large variety of different terrains with varied underlying structure. Based on the experimental observations made in this work, it would thus be ideal to incorporate a higher-level planning algorithm that actively manages the selection of different shape functions, and their associated SBCs, based on a perceived measure of environmental regularity. Several issues will need to be addressed when developing such an algorithm in future work, including how to define a "measure of environmental regularity," how to effectively transition between different controllers/gaits, as well as the inherent tradeoffs in terms of functionality versus computational complexity.

More specifically, in the context of computational complexity, decentralized controllers appear to provide locomotive benefits across a broad range of environmental

conditions and, thus, appear to provide a better, or perhaps more general approach in the experiments considered in this work. However, this work also assumes that the nominal parameters, σ_0 , around which each of the SBCs regulate are given and that the gain matrices, M_d^σ , B_d^σ , and K_d^σ , that determine the compliance of controllers are operator defined and are held fixed. In general, it would be ideal if a higher-level planner could automatically determine these parameters at runtime based on local information about the environment and task specification (e.g. search an area, reach a goal quickly, etc.). Automatically deriving the values of these parameters during operation would make it possible to better control behavioral-level tasks such as determining an optimal forward speed, turning radius, etc. The decentralized controllers inherently incorporate more parameters, meaning that the planning search space would be higher dimensional and, thus, more computationally costly. Thus, by selecting between shape functions that vary in their respective levels of coupling and, thus, in the dimension of their underlying shape parameter spaces, the shape-based approach will provide a potentially intuitive method for implementing a planner with adaptive dimensionality that is similar in concept to those in Gochev et al. (2011, 2012, 2013) in terms of striking a balance between functionality and computational complexity.

Finally, even with an algorithm that selects between shape functions that have different levels of kinematic coupling, there was a limiting and an implicit assumption made in this work that the spatial and temporal phases of the underlying gait patterns, represented by the different shape functions, were fixed. More specifically, each of the SBCs presented in this work controlled only the relative amplitudes of given motions. The controllers could thus *scale up* or *scale down* a nominal motion, but could not actively modify the underlying phasing between the different internal degrees of freedom in the robot (e.g. the hexapod robot's legs were constrained to execute a fixed alternating tripod gait). We partially address this in our current work (Whitman et al., 2016), where we have started to explore how coordination can be incorporated in controllers that compliantly control both phase (spatial as well as temporal) as well as amplitude. In our future work, we will look to more explicitly combine the concepts of shape-based coordination and compliant SBCs with those related to the *dynamic* phase coupling between oscillators typically identified in CPG models.

Funding

The author(s) disclosed receipt of the following financial support for the research, authorship, and/or publication of this article: This work was supported in part by the Robotics Consortium of the U.S Army Research Laboratory under the Collaborative Technology Alliance Program and by the National Science Foundation under Grant No. IIS-1724000.

Notes

- Note that there is a difference in terminology with respect to the definition of a synergy in previous work. In particular, the parameters $\sigma(t)$ are in some cases defined to be synergies.
- The expression in (7) is slightly modified relative to the oscillator output in Ijspeert and Crespi (2007). However, this modification does not change the salient features of the overall CPG model.
- We assume that shape functions in the form (9) are defined for both the desired joint angles θ_d and nominal joint angles θ_0 in (3). We make this assumption throughout this work.
- We assume the nominal shape parameterization σ_0 is constant in (11).
- The shape function in (13) is equivalent to the *modal* shape function in (1).
- Although β_1 and β_2 are linearly independent, we use the more general formulation of the shape-based DMP in (11) in this example.
- If the robot were standing on the ground in this example and a torque was applied about the vertical body axis, the whole-body coupled SBC would cause the robot's body to rotate relative to the static positions of its stance feet. In examples where the robot is walking, i.e. $\omega \neq 0$, applying a torque about the vertical body axis will cause the SBC to compliantly change the robot's heading.
- The example in Figure 5 is included in this section because it demonstrates the static response of the “three windows” SBC included in the experiments presented in Section 5. The reader is referred to the work of Rollinson and Choset (2013) for a more direct demonstration of the practical benefits of decentralized shape control wherein a snake-like robot executing a controller that is similar in concept to a decentralized SBC is shown successfully climbing the outside of a pipe with varying diameter.
- Note that this definition of $\mu_j(t)$ would require an infinite number of windows to track the serpenoid waveform for all time. We present a “recirculation condition” in the definition of $\mu_j(t)$ in (Travers et al., 2016) that addresses this issue.

Supplemental Material

Supplementary video for this article is available online.

References

- Ajoudani A, Godfrey S, Catalano M, Grioli G, Tsagarakis N and Bicchi A (2013) Teleimpedance control of a synergy-driven anthropomorphic hand. In: *IEEE International Conference on Intelligent Robots and Systems*.
- Alexandrov A, Frolov A and Massion J (1998) Axial synergies during human upper trunk bending. *Experimental Brain Research* 118(2): 210–220.
- Burdick J, Radford J and Chirikjian G (1993) A “sidewinding” locomotion gait for hyper-redundant robots. In: *IEEE Conference on Robotics and Automation*.
- Campos R, Matos V and Santos C (2010) Hexapod locomotion: a nonlinear dynamical systems approach. In: *Annual Conference of the IEEE Industrial Electronics Society*.
- Catalano M, Grioli G, Serio A, Farnioli E, Piazza C and Bicchi A (2012) Adaptive synergies for a humanoid robot hand. In: *IEEE Conference on Humanoid Robots*.
- Chirikjian G and Burdick J (1991) Parallel formulation of the inverse kinematics of modular hyper-redundant manipulators. In: *Proceedings IEEE International Conference on Robotics and Automation*.
- Chirikjian G and Burdick J (1994) A modal approach to hyper-redundant manipulator kinematics. *IEEE Transactions on Robotics and Automation* 10(3): 343–354.
- Ciocarlie M, Goldfeder C and Allen P (2007) Dimensionality reduction for hand-independent dexterous robotic grasping. In: *IEEE International Conference on Intelligent Robots and Systems*.
- Date H and Takita Y (2007) Adaptive locomotion of a snake like robot based on curvature derivatives. In: *IEEE/RSJ International Conference on Intelligent Robots and Systems*.
- d’Avella A, Portone A, Fernandez L and Lacquaniti F (2006) Control of fast-reaching movements by muscle synergy combinations. *Journal of Neuroscience* 30(26): 7791–7810.
- Do Carmo M (1976) *Differential Geometry of Curves and Surfaces*. Enlewood Cliffs, NJ: Prentice-Hall.
- Ficuciello F, Palli G, Melchiorri C and Siciliano B (2011) Experimental evaluation of postural synergies during reach to grasp with the UB hand IV. In: *IEEE International Conference on Intelligent Robots and Systems*, pp. 1775–1780.
- Ford S, Rollinson D, Willig A and Choset H (2014) Online calibration of a compact series elastic actuator. In: *American Control Conference (ACC)*.
- Freitas S, Duarte M and Latash M (2006) Two kinematic synergies in voluntary whole-body movements during standing. *Journal of Neuro-physiology* 95(2): 636–645.
- Gabbicini M, Bicchi A, Prattichizzo M and Malvezzi D (2001) On the role of hand synergies in the optimal choice of grasping forces. *Autonomous Robots* 31: 235–252.
- Gelfand J, Lane S and Wilson W (1996) Synergy-based learning of hybrid position/force control for redundant manipulators. In: *IEEE Conference on Robotics and Automation*, April.
- Gochev B K, Cohen, Butzke J, Safonova A and Likhachev M (2011) Path planning with adaptive dimensionality. In: *Fourth Annual Symposium on Combinatorial Search*.
- Gochev K, Safonova A and Likhachev M (2012) Planning with adaptive dimensionality for mobile manipulation. In: *IEEE International Conference on Robotics and Automation*, pp. 2944–2951.
- Gochev K, Safonova A and Likhachev M (2013) Incremental planning with adaptive dimensionality. In: *International Conference on Automated Planning and Scheduling*.
- Godage I, Medrano-Cerda G, Branson D, Guglielmino E and Caldwell D (2015) Modal kinematics for multisection continuum arms. *Bioinspiration and Biomimetics* 10(3): 035002.
- Gong C, Travers M, Kao H and Choset H (2014) Conditioned basis array factorization: An approach to gait pattern extraction. In: *Robotics: Science and Systems*.
- Hauser H, Neumann G and Ijspeert A (2007) Biologically inspired kinematic synergies provide a new paradigm for balance control of humanoid robots. In: *IEEE Conference on Humanoid Robots*.
- Hauser H, Neumann G, Ijspeert A and Maass W (2011) Biologically inspired kinematic synergies enable linear balance control of a humanoid robot. *Biological Cybernetics* 104: 235–249.
- Hirose S (1987) *Biologically Inspired Robots (Snake-like Locomotor and Manipulator)*. Oxford: Oxford University Press.

- Hogan N (1985) Impedance control: An approach to manipulation, part I - Theory. *ASME Journal of Dynamic Systems, Measurement, and Control* 107: 1–7.
- Hogan N and Sternad D (2013) Dynamic primitives in the control of locomotion. *Frontiers in Computational Neuroscience* 7: 1–16.
- Ijspeert A (2008) Central pattern generators for locomotion control in animals and robots: A review. *Neural Networks* 21: 642–653.
- Ijspeert A and Crespi A (2007) Online trajectory generation in an amphibious snake robot using a lamprey-like central pattern generator model. In: *IEEE International Conference on Robotics and Automation*.
- Ijspeert A, Hoffmann H and Schaal S (2013) Dynamical movement primitives: Learning attractor models for motor behaviors. *Neural Computation* 25: 328–373.
- Ijspeert A and Kodjabachian J (1999) Evolution and development of a central pattern generator for the swimming of a lamprey. *Artificial Life* 5(3): 247–269.
- Ijspeert A, Nakanishi J and Schaal S (2002) Movement imitation with nonlinear dynamical systems in humanoid robots. In: *IEEE International Conference on Robotics and Automation*.
- Kamegawa T, Kuroki R, Travers M and Choset H (2012) Proposal of Earli for the snake robot's obstacle aided locomotion. In: *IEEE International Symposium on Safety, Security, and Rescue Robotics*.
- Kano T and Ishiguro A (2013) Obstacles are beneficial to me! Scaffold-based locomotion of a snake-like robot using decentralized control. In: *IEEE/RSJ International Conference on Intelligent Robots and Systems*.
- Lawrence D (1988) Impedance control stability properties in common implementations. In: *IEEE International Conference on Robotics and Automation*, pp. 1185–1190.
- Liljebäck P, Pettersen K, Stavdahl O and Grasdahl J (2011) Experimental investigation of obstacle-aided locomotion with a snake robot. *IEEE Transactions on Robotics* 27(4): 792–800.
- Ott C, Mukherjee R and Nakamura Y (2010) Unified impedance and admittance control. In: *IEEE International Conference on Robotics and Automation*.
- Pinto C (2012) Stability of quadruped robots' trajectories subjected to discrete perturbations. *Nonlinear Dynamics* 70: 2089–2094.
- Prattichizzo D, Malvezzi M and Bicchi A (2006) On motion and force control of grasping hands with postural synergies. In: *Robotics: Science and Systems*.
- Rollinson D, Alwala K, Zevallos N and Choset H (2014a) Torque control strategies for snake robots. In: *IEEE/RSJ International Conference on Intelligent Robots and Systems*.
- Rollinson D, Bilgen Y, Brown B, et al. (2014b) Design and architecture of a series elastic snake robot. In: *IEEE/RSJ International Conference on Intelligent Robots and Systems*.
- Rollinson D and Choset H (2013) Gait-based compliant control for snake robots. In: *IEEE International Conference on Robotics and Automation*.
- Rollinson D, Ford S, Brown B and Choset H (2013) Design and modeling of a series elastic element for snake robots. In: *ASME Dynamic Systems and Controls Conference*.
- Santello M, Flanders M and Soechting J (1998) Postural hand synergies for tool use. *Journal of Neuroscience* 18(23): 10105–10115.
- Schaal S, Kotosaka S and Sternad D (2000) Nonlinear dynamical systems as movement primitives. In: *IEEE-RAS International Conference on Humanoid Robots*.
- Schaal S, Mohajerian P and Ijspeert A (2007) Dynamics systems vs. optimal control—a unifying view. *Progress in Brain Research* 165: 425–445.
- Siciliano B, Sciavicco L, Villani L and Oriolo G (2009) *Robotics: Modelling, Planning, and Control*. New York: Springer.
- Ting L and Macpherson J (2004) A limited set of muscle synergies for force control during a postural task. *Journal of Neurophysiology* (93): 609–613.
- Transth A, Pettersen K and Liljebäck P (2009) A survey on snake robot modeling and locomotion. *Robotics* 27: 999–1015.
- Travers M and Choset H (2015) Shape-constrained whole-body adaptivity. In: *International Symposium on Safety, Security, and Rescue Robotics*.
- Travers M, Whitman J, Schiebel P, Goldman D, and Choset H (2016) Shape-based compliance in locomotion. In: *Robotics: Science and Systems*.
- Tricon V, Le Pellec-Muller A, Martin N, Mesure S, Azulay J and Vernazza-Martin S (2007) Balance control and adaptation of kinematic synergy in aging adults during forward trunk bending. *Neuroscience Letters* 415(1): 81–86.
- Whitman J, Ruscelli F, Travers M and Choset H (2016) Shape-based compliant control with variable coordination centralization on a snake robot. In: *IEEE Conference on Decision and Control*.
- Wimboeck T, Jan B and Hirzinger G (2011) Synergy-level impedance control for a multifingered hand. In: *IEEE Conference on Robotics and Automation*.
- Yamada H and Hirose S (2006) Study on the 3D shape of active cord mechanism. In: *IEEE International Conference on Robotics and Automation*.
- Zhang J, Gao F, Han X, Chen X and Han X (2014) Trot gait design and CPG method for a quadruped robot. *Journal of Bionic Engineering* 11(1): 18–25.

Appendix: Index to multimedia extensions

Archives of IJRR multimedia extensions published prior to 2014 can be found at <http://www.ijrr.org>, after 2014 all videos are available on the IJRR YouTube channel at <http://www.youtube.com/user/ijrrmultimedia>

Table of Multimedia Extension

Extension	Media type	Description
1	Video	Examples demonstrating the performance of SBCs while the phases of different shape functions are continuously varied